

Long-slit spectrophotometry of the multiple knots of the polar ring galaxy IIZw71

E. Pérez-Montero^{1,2}, R. García-Benito³, A.I. Díaz³, E. Pérez¹, and C. Kehrig⁴

¹ Instituto de Astrofísica de Andalucía (CSIC) Apartado de Correos 3004. 18080, Granada, Spain.

e-mail: epm@iaa.es, eperez@iaa.es

² Laboratoire d'Astrophysique de Toulouse et Tarbes, Université de Toulouse, CNRS, 14 avenue E. Belin, 31400 Toulouse, France
e-mail:

³ Departamento de Física Teórica, C-XI, Universidad Autónoma de Madrid, 28049, Cantoblanco, Madrid, Spain
e-mail: ruben.benito@uam.es, angeles.diaz@uam.es

⁴ University of Michigan, Department of Astronomy, 830 Dennison Building, Ann Arbor, MI 48109-1042
e-mail: kehrig@umich.edu

ABSTRACT

Aims. The blue compact dwarf galaxy IIZw71 is catalogued as a probable polar-ring galaxy, and along its long axis it has several very luminous knots showing recent episodes of star formation. Our main aim is to study the physical properties, the stellar content, and the kinematics in the brightest knots of the polar ring

Methods. We carried out long-slit spectroscopic observations of the polar ring in the spectral range 3500 - 10000 Å taken with the William Herschel Telescope (WHT). The spectroscopic observations complemented by the available photometry of the galaxy in narrow H α filters.

Results. We measured the rotation curve of the ring, from which we infer a ratio $M/L_B \approx 3.9$ inside the star-forming ring. We measured the auroral [OIII] line in the two brightest knots, allowing us to measure oxygen, sulphur, nitrogen, argon, and neon chemical abundances following the direct method. Different empirical calibrators were used to estimate the oxygen abundance in the two faintest knots where the temperature sensitive lines could not be measured. The metallicities obtained are very similar for all the knots, but lower than previously reported in the literature from integrated spectra. The N/O abundance, as derived from the N₂O₂ parameter (the ratio of the [NII] and [OII] intensities), is remarkably constant over the ring, indicating that local pollution processes are not conspicuous. Using synthetic stellar populations (SSPs) calculated with the code STARLIGHT, we studied the age distribution of the stellar populations in each knot, finding that in all of them there is a combination of a very young population with less than 10 Myr, responsible for the ionisation of the gas, with other populations older than 100 Myr, probably responsible for the chemical evolution of the knots. The small differences in metallicity and the age distributions among the different knots are indicative of a common chemical evolution, probably related to the process of interaction with the companion galaxy IIZw70. Finally, we calculated the SFR in the different knots from the H α luminosities. The combined SFR rate for the ring amounts to half of the integrated SFR for this galaxy reported by previous authors. The average surface SFR is also higher than the average reported value of HII in polar rings by more than an order of magnitude.

Key words. galaxies : evolution – galaxies : abundances – galaxies : starbursts – galaxies : kinematics and dynamics – galaxies : stellar content

1. Introduction

The intense processes of star formation occurring in the luminous knots of HII galaxies make them easily detected in surveys based on strong emission lines. In fact, these knots present spectra similar to those of HII regions, so it is possible to use them to ascertain the basic properties of the host galaxy, such as extinction, metallicity, star formation rates, and from them derive the chemical evolution and the star formation history of the whole galaxy.

HII galaxies are a subset of blue compact dwarf galaxies (BCDs), which are selected by their compact aspect and blue colour. This type of object is thought to be more frequent in a younger Universe and they are possible building blocks for the largest galaxies that we can detect at low redshifts (Kauffmann et al., 1993). If interactions among dwarf irregular galaxies was a basic mechanism of galaxy formation in the past, it is impor-

tant to study the cases taking place in the nearby Universe now and the links between dwarf interactions and the star formation history of BCDs.

Although IIZw71 is catalogued as a BCD galaxy it is, in fact, characterised by several very luminous H α knots distributed along a ring that is rotating around the host galaxy. It has been catalogued as a probable polar-ring galaxy (B17) in the Polar-Ring Catalogue (Whitmore et al., 1990). Polar ring galaxies (PRGs) are systems with two kinematically separated components. The central component (the host galaxy) is usually a lenticular galaxy or occasionally an elliptical galaxy. The other component, the polar ring, follows a approximately circumpolar orbit around the host and it is characterised by the presence of stars, molecular gas, and dust, inside another bigger ring composed of neutral hydrogen. Thus, this ring becomes an appropriate place for star formation. It is thought that these objects are formed as a consequence of the interaction between galaxies with a small impact parameter (Bournaud & Combes, 2003).

In the case of IIZw71, there are proofs from interferometric observations of interaction with IIZw70, another BCD. In fact, although clearly separated on optical images, both galaxies share a common HI envelope with a gaseous bridge or streamer connecting both structures (see Figure 3 of Cox et al., 2001). This points to an ongoing interaction between the two galaxies. Therefore this system becomes an ideal scenario for studying the effects of interactions in the formation and evolution of BCDs in the Local Universe. A distance of 18.1 Mpc to the system is adopted by Cox et al. (2001), taking a value of $H_0 = 75 \text{ Km s}^{-1} \text{ Mpc}^{-1}$. This implies a linear scale of 90 pc/arcsec on the sky.

In a single long-slit exposition, we have observed the main bursts of star formation along the direction of the polar ring of IIZw71. The analysis of the obtained spectra and the available photometry in several bands were used to make a comparative analysis of the different bursts of star formation. In the next section we describe the long-slit spectroscopic observations of the polar ring of IIZw71. In sect. 3, we present the results of our study, including the determination of physical properties, such as electron density and reddening in the four observed knots, and of chemical abundances in the two brightest knots. In sect. 4, we discuss our results including a study of the kinematics of the polar ring, the determination of metallicity in both the faintest and the brightest knots, the reddening, the stellar properties by means of fitting synthesis stellar populations, and the star formation rates in the individual knots using the available $H\alpha$ photometry of this galaxy. Finally, our conclusions are presented in the last section.

2. Observations and reduction

The long-slit spectrophotometric observations of IIZw71 were obtained using the ISIS double-beam spectrograph mounted on the 4.2m William Herschel Telescope (WHT) of the Isaac Newton Group (ING) at the Roque de los Muchachos Observatory on the Spanish island of La Palma. They were acquired on 2005 July 8 during one single night's observing run and under photometric conditions, with an average seeing of 0.7 arcsec. The EEV12 and Marconi2 detectors were attached to the blue and red arms of the spectrograph, respectively. The R600B grating was used in the blue covering the wavelength range 3670-5070 Å (centred at $\lambda_c = 4370 \text{ Å}$), giving a spectral dispersion of $0.45 \text{ Å pixel}^{-1}$. On the red arm, the R316R grating was mounted in two different central wavelengths providing a spectral range from 5500 to 7800 Å ($\lambda_c = 6650 \text{ Å}$) and from 7600 to 9900 Å ($\lambda_c = 8750 \text{ Å}$) with a spectral dispersion of $0.86 \text{ Å pixel}^{-1}$. To reduce the readout noise of our images, the observations were taken with the 'SLOW' CCD speed. The pixel size for this set-up configuration is 0.2 arcsec for both spectral ranges. The slit width was ~ 1 arcsec, which, combined with the spectral dispersions, yields spectral resolutions of about 1.0 and 3.5 Å FWHM in the blue and red arms, respectively. The instrumental configuration, summarized in Table 1, was planned to cover the whole spectrum from about 3500 to 10000 Å, at the same time providing a moderate spectral resolution. This guarantees the simultaneous measurement of the nebular lines of [OII] $\lambda\lambda 3727, 3729$, and [SII] $\lambda\lambda 9069, 9532 \text{ Å}$ at both ends of the spectrum, in the very same region of the galaxy.

To cover all knots along the polar ring at the same exposure, all the spectra were taken at PA = 30° , an average of 56° off parallactic angle, and the spectra are thus somehow affected by atmospheric differential refraction. Taking the mean air mass into account during the observations of this object (≈ 1.25) and

Table 1. WHT instrumental configuration

Spectral range (Å)	Disp. (Å px ⁻¹)	FWHM (Å)	Spatial res. ('' px ⁻¹)	Exposure Time s
3670-5070	0.45	1.0	0.2	4× 1200
5500-7800	0.86	3.5	0.2	2× 1200
7600-9900	0.86	3.5	0.2	2× 1200

following the curves by Filippenko (1982), we calculated that the displacement between [OII] 3727 Å and [SII] 9069 Å, which are the emission lines the most separated in wavelength, is no greater than 0.9 arcsecs.

Several bias and sky flat field frames were taken at the beginning and at the end of the night in both arms. In addition, two lamp flat fields and one calibration lamp exposure were performed at each telescope position. The calibration lamp used was CuNe+CuAr. The images were processed and analysed with IRAF¹ routines in the usual manner. This procedure includes the removal of cosmic rays, bias subtraction, division by a normalised flat field, and wavelength calibration. Typical wavelength fits were performed using 30-35 lines in the blue and 20-25 lines in the red and polynomials of second to third order. These fits were made at 117 different locations along the slit in each arm (beam size of 10 pixels) obtaining rms residuals between ~ 0.1 and ~ 0.2 pix. In the last step, the spectra were corrected for atmospheric extinction and flux-calibrated. For both arms, two standard star observations were used, allowing a good spectrophotometric calibration with an estimated accuracy of about 5%.

The left panel of Figure 1 shows the spatial distribution of the $H\alpha$ flux along the slit. The emission line profile in this plot has been generated by collapsing 11 pixels of the spectra in the direction of the resolution at the central position of the line in the rest frame, $\lambda 6563 \text{ Å}$. A continuum profile was also generated by collapsing 11 resolution pixels centred at $\lambda 6593 \text{ Å}$. The difference between the two, corresponds to the pure $H\alpha$ emission. It can be seen from the profiles that in knot C, the most intense one, the peaks of the continuum and line emission do not coincide spatially but are separated by 1.6 arcsec. Also the width of the continuum profile is larger than that of the line emission. This suggests that most of this continuum is coming from the host galaxy behind the knot.

The regions of the frames to be extracted into one-dimensional spectra corresponding to each of the knots were selected on the $H\alpha$ line and are marked by horizontal lines in the left panel of Figure 1. In the right panel of the same figure we show the $H\alpha$ image and continuum contours in the R-band from Gil de Paz et al. (2003) in order to illustrate the position of the bursts of star formation and the relative position of the host galaxy. We also show elliptical regions in $H\alpha$ taken to measure the total $H\alpha$ flux of the knots for an aperture correction of the slit measurements. The different emission knots are labelled in both panels.

Figure 2 shows the blue and red parts of the spectra of the four observed knots (labelled from A to D), which have been extracted from the slit. Knot C, as expected, shows the greatest contribution from an underlying stellar population.

¹ IRAF: the Image Reduction and Analysis Facility is distributed by the National Optical Astronomy Observatories, which is operated by the Association of Universities for Research in Astronomy, Inc. (AURA) under cooperative agreement with the National Science Foundation (NSF).

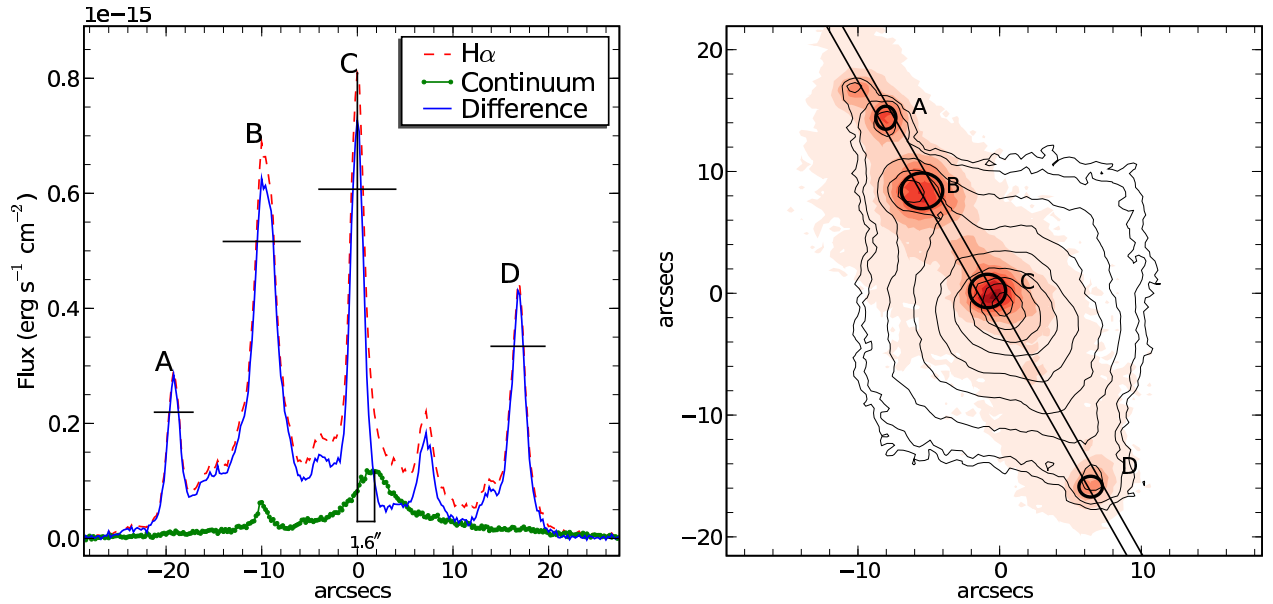


Fig. 1. In left panel, spatial profile of the light distribution along the slit for the observed $H\alpha$ emission (dashed line), the adjacent continuum (**thick green line**), and the difference between the two (**thin blue line**). The horizontal lines show the spatial pixels that have been compressed to produce the one dimensional spectra corresponding to each emission knot. In the right panel, we show the $H\alpha$ image from Gil de Paz et al. (2003) with the identification of the observed knots and the regions for which the broad band magnitudes and the narrow $H\alpha$ flux have been measured. In the same image, we show the position of the slit for the observations described in the text and the elliptical regions measured to correct for aperture effects in each knot. We show the R-band contours as well, as taken from the same source, which show the position of the host galaxy.

3. Results and discussion

3.1. Line intensities and reddening correction

The presence of a conspicuous underlying stellar population depresses the Balmer emission lines and does not allow the measurement of their fluxes with an acceptable accuracy (Díaz, 1988). To account for this, we subtracted from the observed spectra the best-fitting found by the spectral synthesis code STARLIGHT² (Cid Fernandes et al. 2004, 2005; Mateus et al. 2005). STARLIGHT fits an observed continuum spectral energy distribution using a combination of multiple simple stellar population (SSPs; also known as instantaneous burst) synthetic spectra using a χ^2 minimisation procedure. We chose for our analysis the SSP spectra from Bruzual & Charlot (2003), based on the STELIB library of Le Borgne et al. (2003), Padova (1994) evolutionary tracks, and a Chabrier (2003) initial mass function between 0.1 and 100 M_{\odot} . We fixed the metallicity to $Z = 0.004$ ($= 1/5 Z_{\odot}$) for all models, which is the metallicity in the Bruzual & Charlot (2003) library closest to those corresponding to the oxygen abundances measured in knots B and C, as explained in Section 3.3. The code simultaneously finds the ages and the relative contributions of the different present SSPs and the average reddening. The reddening law from Cardelli, Clayton & Mathis (1989) was used. Prior to the fitting procedure, the spectra were shifted to the rest frame, and sampled again to a resolution of 1 Å. Bad pixels and emission lines were excluded from the final fits. The percentage of the mean deviation over all fitted pixels between observed and model spectra ranges between 7.3% in

Table 2. Equivalent widths of the hydrogen recombination lines $H\beta$, $H\gamma$ and $H\delta$ as measured directly in the spectra of the observed knots once the underlying stellar populations have been removed, with the corresponding correction factors.

Knot	A	B	C	D
EW($H\alpha$) (Å)	270±30	130±10	40±2	140±5
f_c	1.00	1.00	1.05	1.00
EW($H\alpha$) _c (Å)	270±30	130±10	42±2	140±5
EW($H\beta$) (Å)	34.9±4.5	30.0±1.7	10.7±1.1	32.2±4.7
f_c	1.01	1.03	1.13	1.00
EW($H\beta$) _c (Å)	35.2±4.7	30.9±1.8	12.1±1.3	32.2±4.9
EW($H\gamma$) (Å)	17.2±1.7	12.8±0.9	5.0±0.9	10.8±1.7
f_c	1.03	1.03	1.19	1.00
EW($H\gamma$) _c (Å)	17.7±1.3	13.2±1.0	6.0±1.0	10.8±0.9
EW($H\delta$) (Å)	8.1±0.6	6.2±0.7	1.8±1.0	8.0±0.8
f_c	1.09	1.13	1.24	1.03
EW($H\delta$) _c (Å)	8.8±0.6	7.0±1.0	2.3±1.0	8.2±1.0

knots A and D, which have the lowest signal, to 2.9 % in knot B and 1.9% in knot C.

Figure 3 illustrates the results of the model fitting to the spectrum of knot C. The upper panel shows the observed spectrum and the model spectrum. The lower panel shows the subtraction of the fitted stellar continuum. We measured the Balmer emission line fluxes over a linear continuum derived by hand from the observed spectra. We then compared these with the same measurements over the continuum derived from the model SSPs. This allows the equivalent widths to be corrected by the presence of absorption stellar features in these lines that cause the measured EWs to be underestimated. In Table 2 we summarise our results for the four brightest Balmer emission lines. For each

² The STARLIGHT project is supported by the Brazilian agencies CNPq, CAPES and FAPESP and by the France-Brazil CAPES/Cofecub program

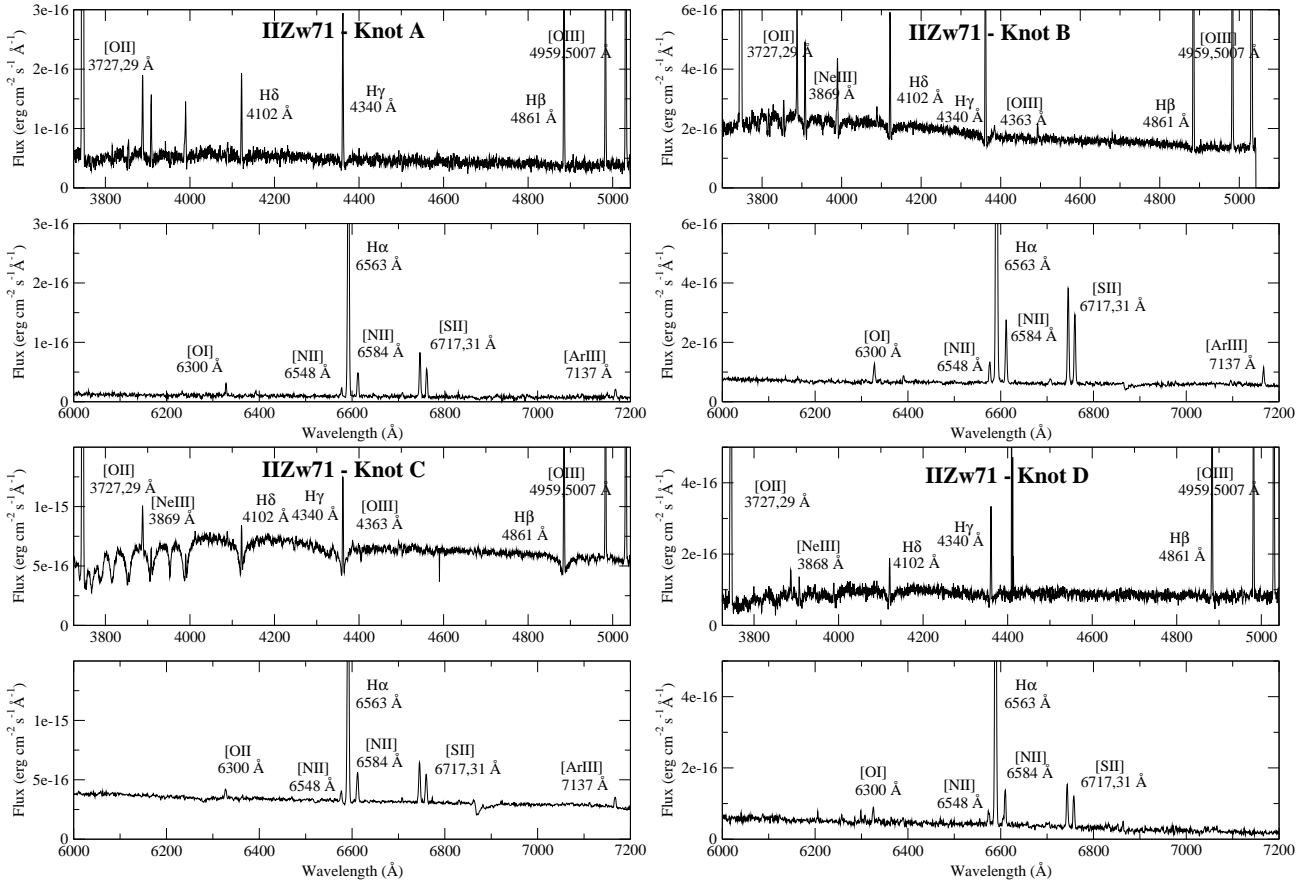


Fig. 2. Blue and red spectra up to 7200 Å for each of the extracted knots of IIZw71.

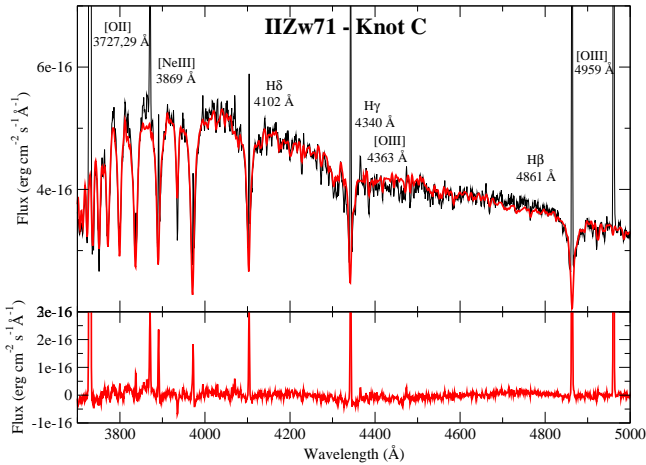


Fig. 3. Results of the STARLIGHT fit to the continuum spectral energy distribution for knot C, the one most affected by underlying stellar population contribution. The lower panel shows the emission line spectrum once this contribution has been removed.

Balmer line, the first row gives the measured equivalent width of the emission line, while the third row gives the corresponding value after the removal of the underlying absorption. The second row gives the ratio between the two. Knot C is the most affected indicating a larger contribution by the underlying stellar population, although the correction for the H β line only amounts to 13%, reaching 24% for the H δ line. For the rest of the knots, only B presents a significant contribution of 13 % for the H δ line.

The emission line fluxes were measured on the spectra using the `splot` task of IRAF and are listed for the four observed knots in Table 3. Column 1 of the table shows the wavelength and identification of the measured lines. The observed emission line fluxes, $F(\lambda)$ (in units of H β flux = 1000) with their corresponding errors, are given in columns 2, 4, 6, and 8 for Knots A, B, C, and D respectively. Only the fluxes of the Balmer recombination lines were measured on the subtracted spectra, while the collisional emission lines were measured on the uncorrected spectra in order to reduce the uncertainties due to the subtraction of the continuum.

We used two different ways to integrate the flux of a given line. (1) In the case of an isolated line, the intensity was calculated by integrating between two points given by the position of a local continuum placed by eye. (2) In the case of the two lines of [OII] at $\lambda\lambda$ 3727, 29 Å, which are partially blended, a multiple Gaussian fit procedure to estimate individual fluxes was used. This procedure is illustrated in Figure 5. The statistical errors associated with the measured emission line fluxes were calculated using the expression

$$\sigma_l = \sigma_c N^{1/2} [1 + EW/(N\Delta)]^{1/2}$$

where σ_l is the error in the measured line flux, σ_c represents the standard deviation in a box near the measured emission line and stands for the error in the continuum placement, N is the number of pixels used in the measurement of the line flux, EW is the line equivalent width, and Δ is the wavelength dispersion in Ångstroms per pixel.

The reddening coefficients ($c(\text{H}\beta)$) were calculated from the measured Balmer decrements, $F(\lambda)/F(\text{H}\beta)$, adopting the galac-

Table 3. Relative observed and reddening corrected line intensities [$F(H\beta)=I(H\beta)=1000$] for the different observed knots of IIZw71. For each knot we also give the flux of $H\beta$, once reddening corrected and after subtraction of the underlying absorption and the constant of reddening, with their corresponding errors.

λ (Å)	A		B		C		D	
	$F(\lambda)$	$I(\lambda)$	$F(\lambda)$	$I(\lambda)$	$F(\lambda)$	$I(\lambda)$	$F(\lambda)$	$I(\lambda)$
3726 [On] ^a	2018±62	2070±240	1545±43	1667±132	1497±60	1561±133	1225±107	1552±227
3729 [On] ^a	2936±289	2767±377	2271±61	2450±163	1990±74	2076±156	1758±150	2227±290
3869 [NeIII]	321±37	328±93	242±23	258±50	297±23	307±53	183±25	224±68
4102 H δ	303±29	307±75	242±15	254±40	257±19	263±42	233±32	270±67
4340 H γ	584±91	570±117	466±13	480±43	483±31	491±52	417±43	458±75
4363 [OIII]	—	—	29±5	30±11	43±10	44±16	—	—
4861 H β	1000±39	1000±39	1000±37	1000±37	1000±47	1000±47	1000±118	1000±118
4959 [OIII]	734±42	733±54	818±27	814±34	937±34	934±41	850±75	837±80
5007 [OIII]	2101±69	2096±99	2411±67	2393±79	2770±95	2759±106	2608±119	2550±223
6300 [OI]	83±19	81±30	92±7	87±16	77±6	74±15	100±13	84±25
6548 [NII]	101±19	99±19	92±7	86±8	93±13	90±17	100±13	82±15
6563 H α	2752±126	2693±269	2895±93	2713±161	3000±120	2894±183	3333±324	2724±320
6584 [NII]	303±21	296±24	250±18	234±21	230±14	222±18	250±15	204±19
6717 [SiII]	514±41	502±59	405±17	378±29	297±12	285±24	267±15	215±29
6731 [SiII]	339±30	332±47	292±12	272±24	217±14	208±24	200±9	161±24
7137 [ArIII]	138±19	134±46	68±7	63±18	77±6	73±20	—	—
9069 [SIII]	92±28	88±42	124±15	110±43	107±14	100±43	250±43	174±80
$F(H\beta)(10^{-15}\text{erg seg}^{-1}\text{cm}^{-2})$	0.89±0.05		3.61±0.10		4.19±0.10		3.49±0.10	
$c(H\beta)$	<0.05		0.09±0.03		0.05±0.02		0.28±0.02	

^a Partially blended (see text and Figure 5)

tic extinction law of Cardelli et al. (1989) with $R_V=3.1$. A least square fit of the measured decrements to the theoretical ones, $(F(\lambda)/F(H\beta))_0$, computed based on the data by Storey & Hummer (1995), was performed that provides the value of $c(H\beta)$. The theoretical Balmer decrements depend on electron temperature and density. We used an iterative method to estimate them, taking as starting values those derived from the measured [SiII] $\lambda\lambda$ 6717,6731 Å and [OIII] $\lambda\lambda$ 4363, 4959, 5007 Å line fluxes.

In Figure 4 we show the actual fits for each of the observed knots. The Galactic extinction for this object is negligible, so we can be sure that internal reddening is the unique source of extinction. All the observed knots present positive values of $c(H\beta)$, except knot A in which the extinction is consistent with zero value. The highest value of $c(H\beta)$ is found for knot D.

The values of $c(H\beta)$ and their corresponding errors, considered as the uncertainties of the least square fits, are listed at the bottom of Table 3 for the observed knots, together with the reddening corrected $H\beta$ intensity. The corrected intensities for the observed lines relative to $H\beta$, $I(\lambda)$, are given in columns 3, 5, 7, and 9 of the same table. In all cases, the reddening correction was done relative to the closest Balmer recombination line.

3.2. Physical conditions of the gas

The physical conditions of the ionized gas, including electron temperatures and electron densities, were derived from the emission line data using the same procedures as in Pérez-Montero & Díaz (2003), based on the five-level statistical equilibrium atom approximation in the task `temden` of the software package IRAF (De Robertis, Dufour & Hunt, 1987; Shaw & Dufour, 1995). The atomic coefficients used here are the same as in Hägele et al. (2006). We took as sources of error the uncertainties associated with the measurement of the emission-line fluxes and the reddening correction and we propagated them through our cal-

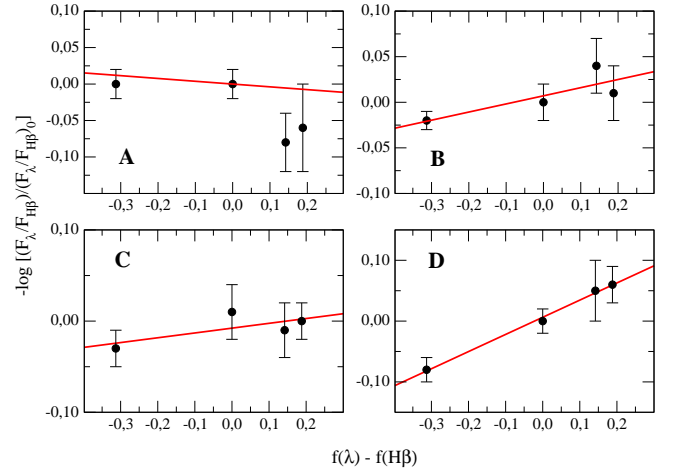


Fig. 4. Representation for each observed knot of the ratio of the expected and observed ratios of the Balmer hydrogen lines and the extinction curve. The slope of the obtained fit is the constant of reddening.

culations. Electron densities were derived in the four knots from both [On] $\lambda\lambda$ 3726/3729 Å and [SiII] $\lambda\lambda$ 6717/6731 Å line ratios, which are representative of the low-excitation zone of the ionized gas. The values for each of the knots are listed in Table 4. In all cases they provide upper limits, which are lower when the [On] lines are used. In the case of these lines, however, the spectral dispersion of our data do not allow total resolution of the lines, and they were deconvolved by fitting two Gaussian components as shown in Figure 5. The upper limits for the electron density are lower in all cases than the critical value.

For knots B and C, for which the intensity of the [OIII] λ 4363 Å was measured with sufficient signal-to-noise (see Figure 6 for a more detailed plot of this line in these knots), the

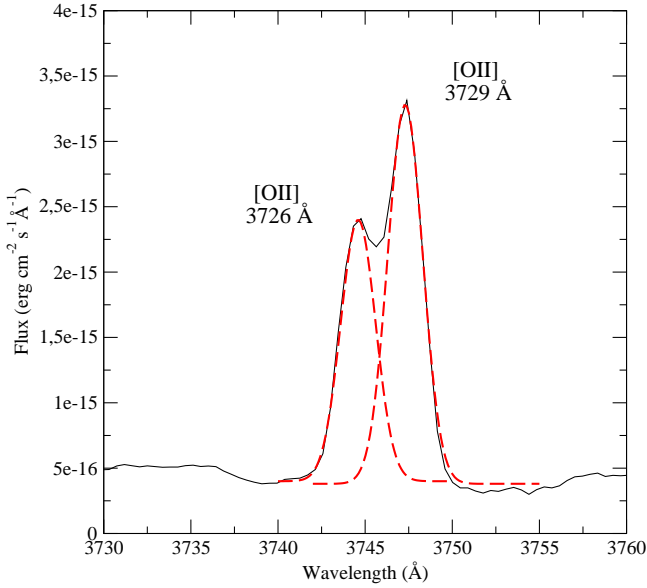


Fig. 5. Deblending of the [OII] $\lambda\lambda$ 3727, 3729 Å lines. Their ratio allows to put lower limits to the electron density in the observed ionized regions.

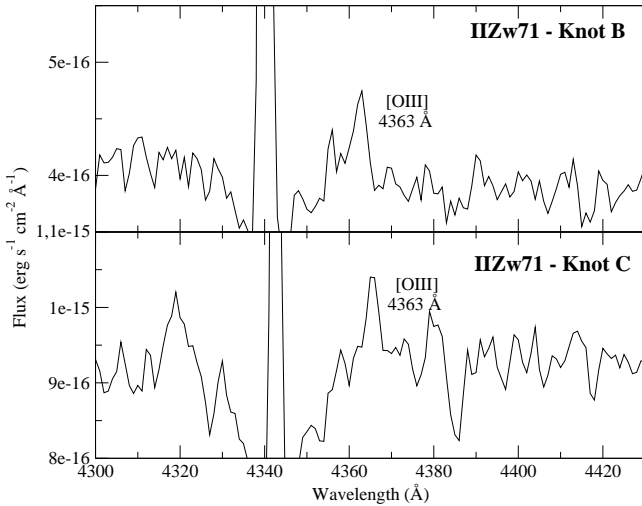


Fig. 6. Detail of the rest-frame spectra of the knots B and C around the [OIII] 4363 Å emission line.

Table 4. Electron densities in particles per cm³ of [SII] and [OII] measured for each of the knots.

Knot	$n([\text{OII}])$	$n([\text{SII}])$
A	<200	<230
B	<85	<160
C	<180	<210
D	<190	<350

[OIII] electron temperature was derived directly from the ratio $(I(4959\text{\AA}) + I(5007\text{\AA})) / I(4363\text{\AA})$. Then we derived $T([\text{OII}])$ from $T([\text{OIII}])$ using the relations based on the photoionization models described in Pérez-Montero & Díaz (2003), which take explicitly into account the dependence of $T([\text{OII}])$ on the electron density, and $T([\text{III}])$ has been estimated from the empirical relation:

$$T([\text{SIII}]) = (1.19 \pm 0.08) T([\text{OIII}]) - (0.32 \pm 0.10)$$

Table 5. Electron temperatures, ionic and total abundances for the knots B and C of IIZw71.

Knot	B	C
$T([\text{OIII}])$	12400 ± 1700 K	13700 ± 2000 K
$T([\text{OII}])^a$	12900 ± 1300 K	12800 ± 1300 K
$T([\text{SIII}])^b$	11600 ± 1100 K	13200 ± 1200 K
$12 + \log(O^+/H^+)$	7.67 ± 0.23	7.63 ± 0.23
$12 + \log(O^{2+}/H^+)$	7.63 ± 0.19	7.57 ± 0.19
$12 + \log(O/H)$	7.95 ± 0.21	7.90 ± 0.21
$12 + \log(S^+/H^+)$	5.94 ± 0.12	5.83 ± 0.13
$12 + \log(S^{2+}/H^+)$	6.00 ± 0.26	5.85 ± 0.26
$\text{ICF}(S^+ + S^{2+})$	1.15 ± 0.13	1.14 ± 0.12
$12 + \log(S/H)$	6.33 ± 0.24	6.20 ± 0.24
$12 + \log(N^+/H^+)$	5.87 ± 0.28	5.63 ± 0.23
$\log(N/O)$	-1.48 ± 0.37	-1.68 ± 0.32
$12 + \log(Ne^{2+}/H^+)$	7.12 ± 0.29	7.06 ± 0.28
$\text{ICF}(Ne^{2+})$	1.22 ± 0.13	1.23 ± 0.14
$12 + \log(Ne/H)$	7.19 ± 0.35	7.13 ± 0.35
$12 + \log(Ar^{2+}/H^+)$	5.61 ± 0.22	5.57 ± 0.19
$\text{ICF}(Ar^{2+})$	1.16 ± 0.03	1.16 ± 0.04
$12 + \log(Ar/H)$	5.65 ± 0.26	5.60 ± 0.26

^a From a relation with $T([\text{OIII}])$ based on photoionization models

^b From an empirical relation with $T([\text{OIII}])$

found by Hägele et al. (2006) for HII galaxies. The values of the derived electron temperatures for these two knots are listed in Table 5.

3.3. Ionic and total chemical abundances in knots B and C.

The oxygen ionic abundance ratios, O^+/H^+ and O^{2+}/H^+ , were derived from the [OII] $\lambda\lambda$ 3727, 3729 Å and [OIII] $\lambda\lambda$ 4959, 5007 Å lines, respectively using the appropriate electron temperatures for each ion. The total abundance of oxygen was derived assuming

$$\frac{O}{H} \approx \frac{O^+ + O^{2+}}{H^+}$$

We derived S^+ abundances from the fluxes of the [SII] emission lines at $\lambda\lambda$ 6717, 6731 Å assuming that $T([\text{SII}]) \approx T([\text{OII}])$ and S^{2+} abundances have been derived from the fluxes of the near-IR [SIII] λ 9069 line and the estimated value of $T([\text{SIII}])$. The total sulphur abundance was calculated using an ionization correction factor (ICF) for $S^+ + S^{2+}$ according to Barker's (1980) formula, which is based on the photoionization models of Stasińska (1978):

$$\text{ICF}(S^+ + S^{2+}) \approx \left[1 - \left(\frac{O^{2+}}{O^+ + O^{2+}} \right)^\alpha \right]^{-1/\alpha}$$

where $\alpha = 2.5$ provides the best fit to the scarce observational data on S^{3+} abundances (Pérez-Montero et al. 2006). Taking this ICF as a function of the ratio O^{2+}/O instead of O^+/O reduces the propagated error for this quantity. The ICF found are similar for the two knots and increase the derived $S^+ + S^{2+}$ by about 15 %.

The ionic abundance of nitrogen, N^+/H^+ , was derived from the intensities of the $\lambda\lambda$ 6548, 6584 Å lines assuming that $T([\text{NII}]) \approx T([\text{OII}])$. Then, the total N abundance was derived under the following assumption:

$$\frac{N}{O} \approx \frac{N^+}{O^+}$$

Neon is only visible in the spectra by means of the [Nem] emission line at $\lambda 3869 \text{ \AA}$. For this ion we took the electron temperature of [OIII], as representative of the high excitation zone. The total abundance of neon was calculated using the following expression for the ICF (Pérez-Montero et al., 2007):

$$ICF(Ne^{2+}) \approx 0.753 + 0.142 \cdot \frac{O^{2+}}{O^+ + O^{2+}} + 0.171 \cdot \frac{O^+ + O^{2+}}{O^{2+}}$$

This formula considers the overestimate of Ne/H in objects with low excitation, where the charge transfer between O^{2+} and H^0 becomes important (Izotov et al., 2004).

The only accessible emission lines of argon in the optical spectra of ionized regions correspond to Ar^{2+} and Ar^{3+} . In the spectra of knot B and C, only [ArIII] $\lambda 7136 \text{ \AA}$ was measured and the abundance of Ar^{2+} was calculated assuming that $T([ArIII]) \approx T([SIII])$ (Garnett, 1992). The total abundance of Ar was then calculated using the $ICF(Ar^{2+})$ derived from photo-ionization models by Pérez-Montero et al. (2007):

$$ICF(Ar^{2+}) = 0.749 + 0.507 \cdot \left(1 - \frac{O^{2+}}{O^+ + O^{2+}}\right) + 0.0604 \cdot \left(1 - \frac{O^{2+}}{O^+ + O^{2+}}\right)^{-1}$$

The calculated ICF for Ar and Ne are the same in the two knots within the errors. The ionic and total abundances for the observed species in knots B and C are given in Table 5, along with their corresponding errors.

3.4. Metal content of the polar ring

The emission-line spectra of the four star-forming knots in IIZw71 are remarkably similar, implying similar values for ionization parameter, ionization temperature, and chemical abundances. We derived the ionization parameters from the ratio of the [OII] and [OIII] lines according to the expression given in Díaz et al. (2000). They are similar in all the knots ranging from 6.42×10^{-4} for knot A to 9.67×10^{-4} for knot C. Using these values, the corrected $H\alpha$ fluxes, and the sizes of the regions from $H\alpha$ images we can calculate the density of the emitting gas (Díaz et al. 1991). This is similar for the four knots with a value of about $20 \text{ particles} \cdot \text{cm}^{-3}$, consistent with the upper limits we derived from the ratio of the [SII] lines and providing filling factor for the gas of a few times 10^{-2} , values common to giant HII regions.

We derived oxygen, sulphur, nitrogen, neon, and argon chemical abundances in knots B and C, where the auroral line of [OIII] at 4363 \AA had been measured and thus the electron temperature of the high-excitation zone also was derived. We assumed also an inner structure of the electron temperature to deduce the values of the temperatures of [OII], which is representative of the low-excitation zone, affecting the calculation of the chemical abundances of O^+ , N^+ , and S^+ . This inner ionization structure leads to derivation of the temperature of [SIII], valid for the intermediate zone (Garnett, 1992) and calculation of the ions of S^{2+} and Ar^{2+} . The derived ionic abundances in these two knots are very similar, leading to total O/H abundances of $12 + \log(O/H) = 7.90$ in knot C and 7.95 in knot B. These values deviate slightly from the metallicity reported in the literature for the integrated object, which is $12 + \log(O/H) = 8.24$ (Shi et al., 2005; Kewley et al., 2005) and the difference is even greater than the value for the nuclear region, which could be considered as knot C, given by Kewley et al. (2005), which is $12 + \log(O/H) = 8.55$. The value

reported by Shi et al. (2005) are based on the direct method, while those reported by Kewley et al. (2005) were derived using empirical calibrations since no temperature sensitive lines were observed.

This is also the case in our observations of knots A and D. The calculation of metallicities in these two knots can only be carried out with calibrations based on the strongest emission lines because no auroral lines were detected and the direct method cannot be used.

The different strong-line methods for abundance derivations, which have been widely studied in the literature, are based on the directly calibrating of the relative intensity of some bright emission lines against the abundance of some relevant ions present in the nebula. For the case of oxygen, we take the calibrations studied by Pérez-Montero & Díaz (2005), who obtain different uncertainties for each parameter in a sample of ionized gaseous nebulae with accurate determinations of chemical abundances in the whole range of metallicity.

In Figure 7, we show the corresponding total abundances as derived from several strong-line methods and the oxygen abundances calculated from the electron temperatures measured in knots B and C. Among the available strong-line parameters we studied the O_{23} parameter (also known as R_{23} and originally defined by Pagel et al. (1979) and based on [OII] and [OIII] strong emission lines). This parameter is characterised by its double-valued relation with metallicity, with a very large dispersion in the turnover region. According to the values measured in knots B and C, we used the McGaugh (1991) calibration for the lower branch, obtaining similar values for the oxygen abundance in the four observed knots.

The $N2$ parameter (defined by Storchi-Bergmann et al., 1994) is based on the strong emission lines of [NII]. It remains single-valued up to high metallicities in its relation to oxygen abundance, and it is almost independent of reddening and flux calibrations. Nevertheless, it has the high dispersion associated to the functional parameters of the nebula (ionization parameter and ionizing radiation temperature) and to N/O variations. We used the empirical calibration of this parameter from Denicoló et al. (2002) to derive the oxygen abundance in the four knots of this galaxy. We can see in Figure 7 that the abundances predicted by this parameter are quite similar for all the knots although more than the values derived from the direct method in knots B and C.

The S_{23} parameter was defined by Vílchez & Esteban (1996) and is based on the strong emission lines of [SII] and [SIII]. The calibration done by Pérez-Montero & Díaz (2005) yields oxygen abundances comparable to the four observed knots, slightly higher than the directly derived abundances of knots B and C, but still consistent with them within the errors. In the case of sulphur, both the directly and empirically derived abundances of knots B and C are slightly different with knot C showing a lower abundance. However it should be remembered that the near IR sulphur lines relative to the hydrogen recombination lines are more affected by reddening than in the case of oxygen when no Paschen lines are observed, which is the case.

The parameter $O3N2$, defined by Alloin et al. (1979) depends on strong emission lines of [OIII] and [NII]. We used the calibration due to Pettini & Pagel (2004) and, as we can see in Figure 7 it has a very similar behaviour to that of $N2$.

The combination of the S_{23} and O_{23} parameters gives S_{23}/O_{23} , defined by Díaz & Pérez-Montero (2000), a parameter that increases monotonically with the oxygen abundance up to oversolar regime and which is very useful to study variations over wide ranges of metallicity (*e.g.* disks). We applied the cali-

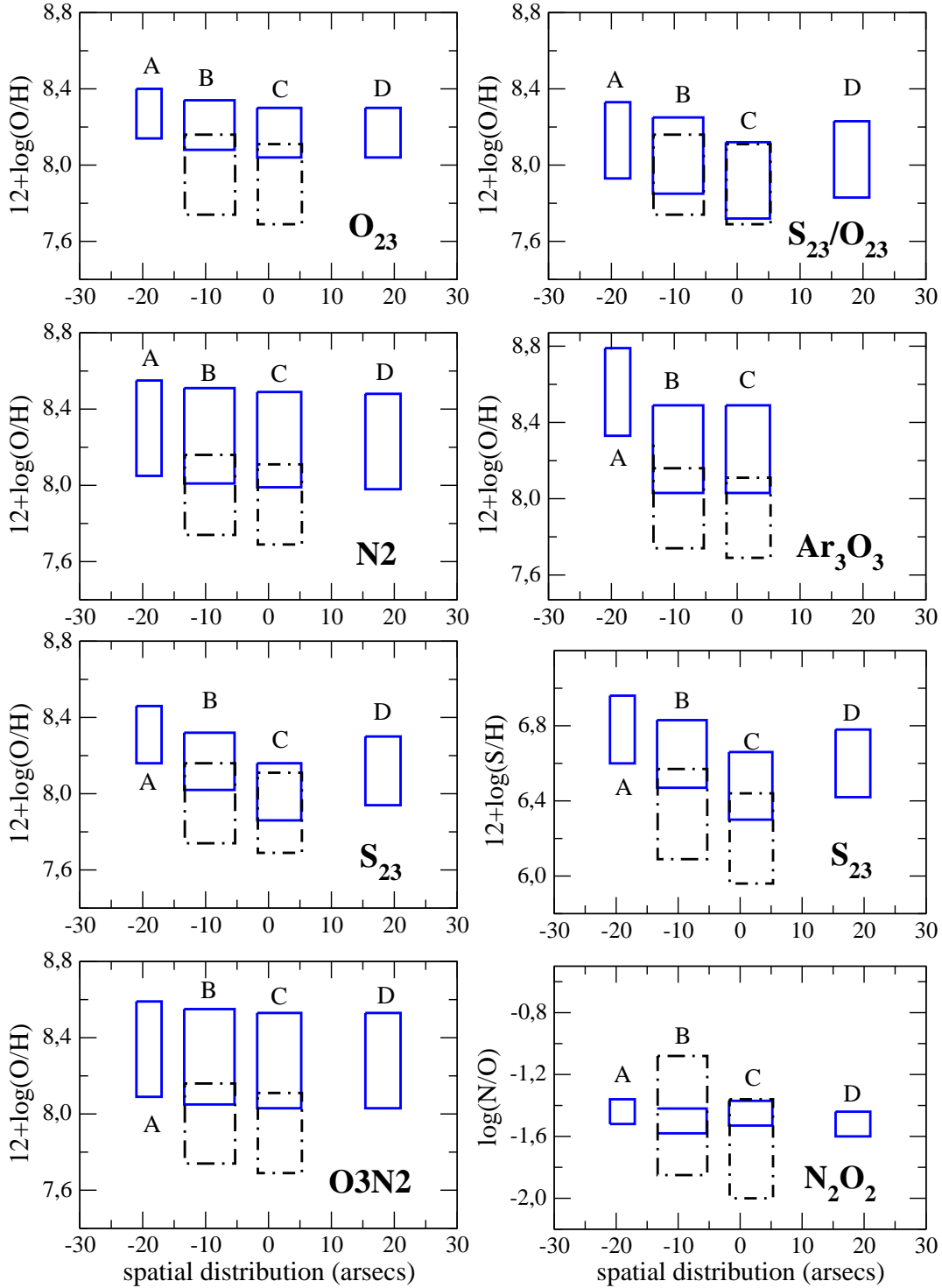


Fig. 7. The oxygen abundances and their uncertainties for each observed knot, as derived using different empirical calibrators. From upper to lower panel: O_{23} , N_2 , S_{23} and $O3N2$, at left and Ar_3O_3 and S_{23}/O_{23} at right. The lower panels of right column represent the sulphur abundance as derived from the S_{23} parameter and the N/O ratio as derived from the N_2O_2 parameter. The dash-dotted line represent the abundances and their uncertainties as derived from the direct method in knots B and C.

bration found in Pérez-Montero & Díaz (2005) and, in this case, there is almost a perfect coincidence with the values found by the direct method in knots B and C. Again, we find a similar value in knots D and A.

The Ar_3O_3 parameter, defined and calibrated by Stasińska (2006) as the ratio of $[ArIII]$ 7136 Å and $[OIII]$ 5007 Å emission lines, predicts identical values for the metallicity in knots B and

C, although noticeably higher than the directly derived ones. A rather high value is found in knot A and no data on the $[ArIII]$ line in knot D were available.

Finally, the N_2O_2 parameter, defined by Pérez-Montero & Díaz (2005) as the ratio between $[NII]$ and $[OII]$ emission lines, can be used to obtain the N/O ratio. Using this parameter, very

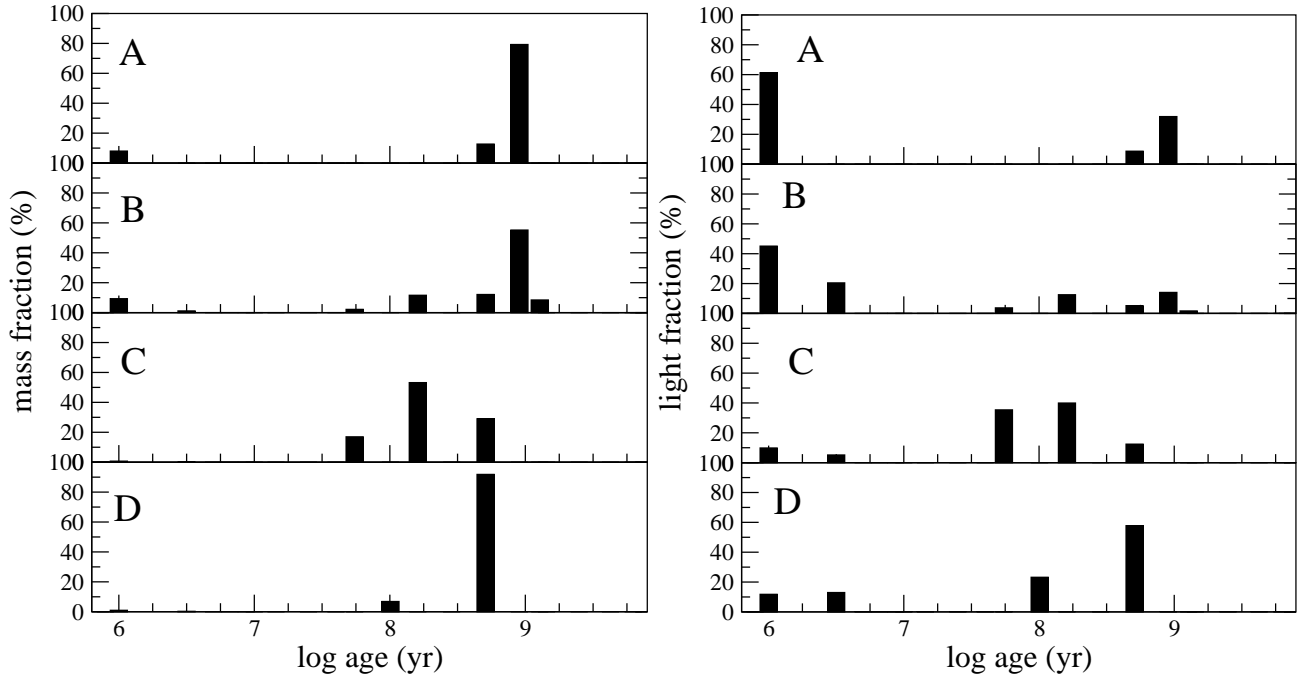


Fig. 8. Histogram of the distribution in mass fraction (left) and visual light (right) of the most probable stellar population models fitted by STARLIGHT for each of the observed knots.

Table 6. Values of the extinction, total stellar mass, and fraction of the mass in stars younger than 10 Myr for each knot in the best-fit model predicted by STARLIGHT.

ID	$c(H\beta)$	$\log (M/M_{\odot})$	$f(\text{age} < 10 \text{ Myr})$
A	0.19	6.13 ± 0.05	0.08
B	0.46	6.92 ± 0.05	0.11
C	0.04	7.52 ± 0.04	0.008
D	0.25	6.46 ± 0.04	0.013

little difference is found in N/O among the four observed knots, which are also consistent with the directly derived ratio.

3.5. The stellar population

The study of the stellar content in the four observed knots was carried out using STARLIGHT code, which calculates the combination of stellar libraries and the extinction law that reproduce the spectral distribution of energy, to derive the properties of the stellar population in each of the knots better. The used Population Synthesis stellar libraries and the method to fit the observed spectra of each of the knots in the polar ring is described in Sect. 3.1.

In Figure 8 we show the age distributions of the mass fraction (left) and the visual light fraction (right) for the four knots. All of them present a very young stellar populations with ages below 10 Myr, responsible of the ionization of the surrounding gas, although most of the stellar mass belongs to populations older than 100 Myr in almost all cases. The estimated total stellar mass and the fraction by mass of the stellar population with an age younger than 10 million years, responsible for the ionization of the gas, are listed in Table 6 for all the knots, together with the internal extinction, represented by the reddening constants, estimated by the model. The masses were corrected using an aperture factor, which takes into account the light not collected by the slit and which was calculated as the weighted mean

of the ratios of the light in the whole region as measured in the $H\alpha$ image and in the regions covered by the slit.

Although it is not expected to find the same values of extinction in the gas and the stellar population, there is a very good agreement between the values of the extinction estimated by STARLIGHT in knots C and D in relation to the values obtained from the decrement of Balmer. In knots A and B, the values are higher than those derived for the ionized gas. In these two knots the specific weight of the youngest population is higher. Since STARLIGHT assumes a common source of extinction for all the stellar populations entering the fit, the degeneracy between age and extinction tends to overestimate the extinction derived for the optimal fit. On the other hand, in knots C and D, which are probably contaminated by the light coming from the host galaxy, the contribution by the young stellar population is much lower, and the light at longer wavelengths is dominated by the older stellar population and the estimated average extinction is more representative.

3.6. Ionising stellar populations

Some properties of the emission knots can be obtained from the measured $H\alpha$ flux, such as $H\alpha$ luminosity, number of ionising photons, mass of ionising stars and mass of ionised hydrogen (see Díaz et al. 2000). In order to obtain these quantities, we analysed the $H\alpha$ image of the galaxy, retrieved from the Palomar/Las Campanas atlas of blue compact dwarf galaxies (Gil de Paz et al., 2003). We defined elliptical apertures on this image for each of the four knots extracted in the spectroscopic observations and we measured all the flux inside the elliptical apertures up to the isophote corresponding to the 30% of the light in the brightest knot. These regions are shown in the right panel of Figure 1, and their sizes are given in the first column of Table 7, as the radius of a circular aperture of area equal to that encompassed by the refereed isophote. The observed $H\alpha$ flux

Table 7. Derived properties of the observed knots using the extinction-corrected $H\alpha$ fluxes measured in the images from Gil de Paz et al. (2003).

ID	R_{eq} (arcsec)	$I(H\alpha)$ $10^{-14} \text{ erg} \cdot \text{s}^{-1} \cdot \text{cm}^{-2}$	$L(H\alpha)$ $(10^{38} \text{ erg} \cdot \text{s}^{-1})$	$Q(H^0)$ $(10^{51} \cdot \text{s}^{-1})$	M_{ion} $(10^5 \cdot M_\odot)$	$M(HII)$ $(10^4 \cdot M_\odot)$	SFR M_\odot/yr
A	1.64	1.25	4.91	3.59	7.16	3.64	0.004
B	2.94	4.83	19.0	13.9	27.6	14.1	0.015
C	2.65	3.96	15.6	11.4	22.7	11.5	0.012
D	1.43	1.10	4.33	3.16	6.31	3.21	0.003

was corrected in each knot for reddening using the values of the reddening constants, $c(H\beta)$, given in Table 3. The derived values are given in Table 7.

The derived values of the masses of the ionising clusters can be compared with those provided by the STARLIGHT fit. STARLIGHT gives lower values than the ones we derive by factors between 6 and 8 for knots A, B and, C. In the case of knot D, the difference is more than an order of magnitude. If we take the masses derived from the $H\alpha$ fluxes, which are, in principle, lower limits since neither dust absorption nor a possible escape of photons are taken into account, and we use the calculated proportions of young to total mass given in Table 6 we obtain total masses between 0.9×10^7 and $4.9 \times 10^7 M_\odot$ for knots A, B and, D and $2.8 \times 10^8 M_\odot$ for knot C. This high value points to a large contribution to the older population by the bulge of the host galaxy. This is consistent with the continuum light distribution shown in Figure 1 which is wider than that associated with cluster C and peaks at a region displaced from that of the cluster by 1.6 arcsec (about 144 pc). On the other hand for knot B the cluster shows a significant continuum of the same spatial extent as the line emission and the maxima of both distributions coincide. Knots A and D show very little continua of their own, so their underlying population probably corresponds to the outer parts of the host galaxy.

Since the differences in metallicity among the different knots are not significant and the age distributions are also similar, this could indicate a common chemical evolution of these knots, probably related to the process of interaction with the companion galaxy IIZw70.

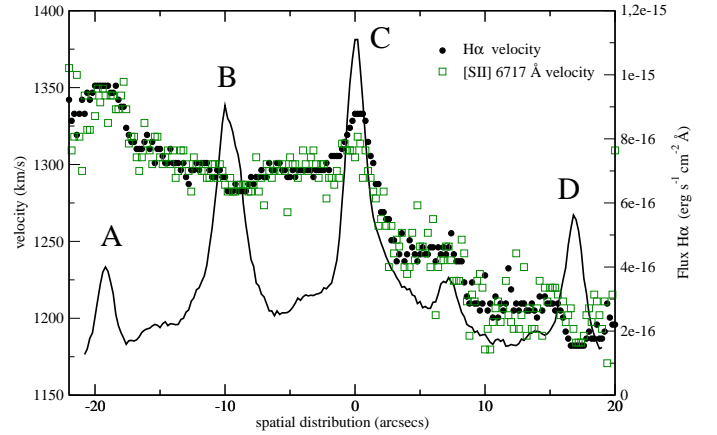
The star formation rate (SFR) for each knot was derived from the $H\alpha$ luminosity using the expression given by Kennicutt (1998):

$$SFR = 7.9 \times 10^{-42} \times L(H\alpha)$$

. The derived values are also given in Table 7. They vary from $0.003 M_\odot \text{ yr}^{-1}$ for knot D to $0.015 M_\odot \text{ yr}^{-1}$ for knot B and provide a total SFR for the ring of $0.035 M_\odot \text{ yr}^{-1}$, about half of the values quoted by Kewley et al. (2005) for the integrated object, which is $0.066 M_\odot \text{ yr}^{-1}$. Using the sizes of the emitting regions obtained from the $H\alpha$ images and listed in Table 7, we obtain a rather constant SFR per unit area, of the order of $7 \times 10^{-8} M_\odot \text{ yr}^{-1} \text{ pc}^{-2}$. This is higher than the average value of individual HII regions in polar rings given in Reshetnikov & Combes (1994) which is $3.2 \times 10^{-9} M_\odot \text{ yr}^{-1} \text{ pc}^{-2}$.

3.7. Kinematics and dynamics of the polar ring

We have analysed the differential radial velocity along the slit using the $H\alpha$ and [Sn] 6717 Å emission lines. The heliocentric velocities are displayed in Figure 9 superimposed on the observed $H\alpha$ profile. We find an asymmetric rotation, as it was already stated by Reshetnikov & Combes (1994), possibly affected by

**Fig. 9.** Rotation curve of IIZw71. Filled circles represent heliocentric velocity derived from $H\alpha$ and open squares from [Sn] 6717 Å. Solid line represents the spatial distribution of flux of $H\alpha$ to be compared with the rotation curve.

the expanding velocities of the bubbles of ionised gas surrounding the knots of star formation which reaches 60 km/s in the case of knot C.

Assuming that we see the polar ring of the galaxy edge-on, with a radial velocity of 85 km/s, and considering an optical radius of 20 arcsec, which is where we can measure the emission lines with a good enough signal-to-noise ratio, we calculated a dynamical mass inside this radius of $(2.8 \pm 0.2) \times 10^9 M_\odot$. We then calculated the L_B luminosity inside the radius of 20 arcsec, internal to the polar ring, from the B brightness distribution given in Cairos et al. (2001), obtaining $L_B = 7.2 \times 10^8 L_\odot$. Therefore, we obtain a value of 3.9 for the M/L_B ratio inside the star forming-ring. This is close to the value of 2.8 found by Reshetnikov & Combes (1994) from optical observations within a distance of 30 arcsec from the centre. Considering that their considered blue light probably encompasses the light coming from the emission knots in the ring, that luminosity probably constitutes an upper limit and provides a lower limit to the M/L_B .

4. Summary and conclusions

Spectrophotometric observations of the galaxy IIZw71 were carried out to study the physical properties of the bursts of star formation along its polar ring. We extracted information on the four brightest knots in $H\alpha$ that we labelled from A to D.

The electron temperature of [OIII] was measured in knots B and C, allowing the direct derivation of ionic abundances of oxygen, sulphur, nitrogen, neon and argon. The total abundances of these species are in the same range of metallicities measured in HII galaxies, but they are slightly lower than the abundances previously reported from measurements of the integrated galaxy according to strong-line calibrations. The metallicity in the other

two fainter knots, where the temperature sensitive line could not be detected, was estimated by means of different strong-line parameters. In all cases, the estimated abundances are consistent with those derived for knots B and C by the direct method with the parameter involving the sulphur lines providing the abundance closer to it. The rest of the parameters slightly overestimate the oxygen abundance. The N/O abundance, as derived from the N_2O_2 parameter (the ratio of the [NII] and [OII] intensities), is remarkably constant over the ring indicating that local pollution processes are absent.

Although the underlying stellar population of the host galaxy is detected in the spectrum of the central knot (knot C), the similarity of the star formation histories in the four knots, as deduced from the fitting of SSPs, as well as the derived metallicities, point to a common chemical evolution of the polar ring.

We calculated the SFR in the different knots studied from the $H\alpha$ luminosities. The combined SFR for the ring amounts to half of the integrated SFR for this galaxy reported by previous authors. The average SFR is also higher than the average reported value for HII regions in polar rings by more than an order of magnitude.

Finally, for the differential velocity, we used the wavelength position of $H\alpha$ and [SII] to measure an asymmetric rotation of the ring with a mean value of 85 km/s at an optical radius of $20''$. This gives a dynamical mass of $(2.8 \pm 0.2) \cdot 10^9 M_\odot$ and an M/L_B ratio of 3.9, close to the value reported previously by Reshetnikov & Combes (1994). The kinematics of the ring is significantly affected by the expanding bubbles of ionised gas, which in the case of knot C reaches 60 km/s.

Acknowledgements. This work has been partially supported by projects AYA2004-02703, AYA2007-67965-C03-02, AYA2007-67965-C03-03, and AYA2007-64712 of the Spanish National Plan for Astronomy and Astrophysics and the CNRS-INSU and its Programmes Nationaux de Galaxies et de Cosmologie (France). Also, partial support from the Comunidad de Madrid under grant S0505/ESP000237 (ASTROCAM) is acknowledged. EPM acknowledges his financial support from the *Fundación Española para la Ciencia y la Tecnología* during his two-year postdoctoral position in the LATT/OMP.

The WHT is operated on the island of La Palma by the ING in the Spanish Observatorio del Roque de los Muchachos of the Instituto de Astrofísica de Canarias. We thank the Spanish allocation committee (CAT) for awarding observing time.

We would like to thank to Armando Gil de Paz, for allowing the study of B, R, and $H\alpha$ images of IIZw71 in the Palomar/Las Campanas Atlas of Blue Compact Galaxies and to Guillermo F. Hägele for very interesting discussions and comments that have helped to improve this work. We thank Roberto Cid Fernandes and the people of the Starlight Project Team (UFSC, Brazil), for making the STARLIGHT code available. We also thank the anonymous referee for his/her constructive comments.

References

Alloin, D., Collin-Souffrin, S., Joly, M., & Vigroux, L. 1979, *A&A*, 78, 200
 Barker, T. 1980, *ApJ*, 240, 99.
 Bournaud, F., & Combes, F. 2003, *A&A*, 401, 817
 Bruzual, G., & Charlot, S. 2003, *MNRAS*, 344, 1000
 Cairós, L. M., Vílchez, J. M., González Pérez, J. N., Iglesias-Páramo, J., & Caon, N. 2001a, *ApJS*, 133, 321
 Cairós, L. M., Caon, N., Vílchez, J. M., González-Pérez, J. N., & Muñoz-Tuñón, C. 2001b, *ApJS*, 136, 393
 Cardelli, J. A., Clayton, G. C., & Mathis, J. S. 1989, *ApJ*, 345, 245
 Chabrier, G. 2003, *PASP*, 115, 763
 Cid Fernandes, R., Gu, Q., Melnick, J., Terlevich, E., Terlevich, R., Kunth, D., Rodrigues Lacerda, R., & Joguet, B. 2004, *MNRAS*, 355, 273
 Cid-Fernandes, R., Mateus, A., Sodr , L., Stasińska, G. & Gomes, J.M. 2005, *MNRAS*, 358, 363.
 Cox, A.L., Sparke, L.S., Watson, A.M., von Moorsel, G. 2001, *AJ*, 121, 692.
 Denicol , G., Terlevich, R., & Terlevich, E. 2002, *MNRAS*, 330, 69
 De Robertis, M.M., Dufour, R.J. & Hunt, R.W. 1987, *JRASC*, 81, 195
 D az, A. I. 1988, *MNRAS*, 231, 57

D az, A. I., & P rez-Montero, E. 2000, *MNRAS*, 312, 130
 D az, A. I., Castellanos, M., Terlevich, E. & Garc a-Vargas, M.L. 2000, *MNRAS*, 318, 462
 Filippenko, A. V. 1982, *PASP*, 94, 715
 Garnett, D.R. 1992, *AJ*, 103, 1330.
 Gil de Paz, A., Madore, B.F. & Pevunova, O. 2003, *ApJSS*, 147, 29.
 H gele, G. F., P rez-Montero, E., D az,  . I., Terlevich, E., & Terlevich, R. 2006, *MNRAS*, 372, 293
 Izotov, Y. I., Stasińska, G., Guseva, N. G., & Thuan, T. X. 2004, *A&A*, 415, 87
 Kauffmann, G., White, S.D.M. & Guiderdoni, B. 1993, *MNRAS*, 264, 201
 Kennicutt, R. C., Jr. 1998, *ARA&A*, 36, 189
 Kewley, L., J., Jansen, R.A. & Geller, M.J. 2005, *PASP*, 117, 227
 Le Borgne, J.-F., et al. 2003, *A&A*, 402, 433
 Mateus, A., Sodr , L., Cid Fernandes, R., Stasińska, G., Schoenell, W., & Gomes, J. M. 2006, *MNRAS*,
 McGaugh, S. S. 1991, *ApJ*, 380, 140
 Pagel, B. E. J., Edmunds, M. G., Blackwell, D. E., Chun, M. S., & Smith, G. 1979, *MNRAS*, 189, 95
 P rez-Montero, E. & D az, A.I. 2003, *MNRAS*, 346, 105.
 P rez-Montero, E. & D az, A.I. 2005, *MNRAS*, 361, 1063.
 P rez-Montero, E., D az, A. I., V lchez, J. M., & Kehrig, C. 2006, *A&A*, 449, 193
 P rez-Montero E., H gele G. F., Contini T., D az  . I., 2007, *MNRAS*, 381, 125
 Pettini, M., & Pagel, B. E. J. 2004, *MNRAS*, 348, L59
 Reshetnikov, V.P. & Combes, F. 1994, *A&A*, 291, 57.
 Shaw, R. A., & Dufour, R. J. 1995, *PASP*, 107, 896
 Shi, F., Kong, X., Li, C., & Cheng, F. Z. 2005, *A&A*, 437, 849
 Stasińska, G. 1978, *A&A*, 66, 257.
 Stasińska, G. 2006, *A&A*, 454, L127
 Storchi-Bergmann, T., Calzetti, D., & Kinney, A. L. 1994, *ApJ*, 429, 572
 Storey, P. J., & Hummer, D. G. 1995, *MNRAS*, 272, 41
 V lchez, J.M. & Esteban, C. 1996, *MNRAS*, 280, 720.
 Whitmore, B.C., Lucas, R.A., McElroy, D.B., Steiman-Cameron, T.Y., Sackett, P.D. & Olling, R.P. 1990, *AJ*, 100, 1489.